TURUN YLIOPISTON JULKAISUJA
ANNALES UNIVERSITATIS TURKUENSIS

SARJA - SER. A I OSA - TOM. 454

ASTRONOMICA - CHEMICA - PHYSICA - MATHEMATICA

FRAGMENTATION PROCESSES IN ORGANIC MOLECULES INDUCED BY SYNCHROTRON RADIATION

by

Eero Itälä

TURUN YLIOPISTO
UNIVERSITY OF TURKU
Turku 2012

From

Department of Physics and Astronomy
University of Turku
FI-20014 Turku
Finland

Supervised by

PhD. Sari Granroth and Professor Edwin Kukk
Laboratory of Materials Science
Department of Physics and Astronomy
University of Turku
Finland

Reviewed by

Professor Stacey Sörensen
Department of Physics
Lund, Sweden
Lund University

PhD. Lorenzo Avaldi
CNR-institutio di Metodologie
Inorganiche e dei Plasmi
Monterotondo, Italia

Opponent

Nora Berrah
Professor
Physics Department
Western Michigan University
Kalamazoo, USA

ISBN 978-951-29-5279-3 (PRINT)
ISBN 978-951-29-5280-9 (PDF)
ISSN 0082-7002
Suomen Yliopistopaino Oy – Juvenes Print – Turku, Finland 2013

Acknowledgements

I would, first of all, like to thank Professor Edwin Kukk who introduced the fascinating world of molecular physics to me and who has always found time for my guidance. I am also grateful to Doctor Sari Granroth who encouraged me to start my PhD studies and who has supported me during the past years. Thank you Doctor Kuno Kooser for often doing the dirty work and Mr Dang Trinh Ha for elucidating discussions and your everlasting patience. My dear colleagues at the laboratory of materials science, Jarkko Leiro, Markku Heinonen, Taina Laiho and Helena Levola, you are the best.

Thank you Professor Elisabeth Rachlew and Doctor Michael Huels for the fun beamtimes and for your constructive comments concerning my papers. Working with has been a privilege. I would also like to thank Professor Ergo Nõmmiste, Doctors Samuli Urpelainen, Leena Partanen and Antonio Caló as well as Mr Urmas Joost for their help and company during the beamtimes.

I thank Professor Stacey Sörensen and Doctor Lorenzo Avaldi for reviewing my thesis and for constructive comments. The financial support from the Graduate School for Materials research (GSMR), the Doctoral Programme in Nanoscience (NGS-NANO), University of Turku Graduate School UTUGS, Emil Aaltonen foudation and the scholarship fund of Wäinö Edward Miettinen is acknowledged. The help of the staff of Max lab during the beamtimes is also acknowledged.

Finally, I want to thank my parents for giving me the gift of life and my brothers (of the past) as well as all my friends for the numerous adventures during the past years. My most sincere thanks goes to my beloved wife Laura and my son Risto, you are the light of my life.

Contents

Abstract

This thesis presents studies on fragmentation processes of relatively simple organic molecules following valence and core excitations, the emphasis being on fragmentation processes of core ionized molecules into pairs of cations. The experimental technique combines electron- and ion spectroscopy with synchrotron radiation and is called the electron energy resolved PhotoElectron-PhotoIon-PhotoIon COincidence (PEPIPICO) technique. The PEPIPICO technique allows not only the detection of momentum correlated ion pairs and the corresponding electron originating from the same ionization event, but also very detailed description of the dissociation process and the determination of kinetic energy released in the process.

In addition to the detailed determination of the fragmentation processes, also the effects of the initial geometry of the sample, chemical environment and the initial ionization site has been studied. The consideration of the initial ionization site was possible due to the energy resolved electron detection of the measurement equipment and the chemical shifts caused by the different environments of the core ionized atoms. Different ionization sites show as separate photolines in the XPS spectra measured in coincidence with the photoions. The dependence of fragmentation on the initial ionization site was investigated by selecting a certain photoline and considering only those photoions corresponding to the selected photoline. The results show that core ionization induces a large variety of fragmentation processes, most of which take place in separate sequential steps. Chain molecules often fragment into just two singly charged fragments, whereas cyclic molecules favor fragmentation processes producing more than two fragments. Although the fragmentation depends very little on the initial ionization (core hole) site, the coincident measurements with resonant Auger electrons showed that the electronic final state *i*.e. the final valence hole(s) effect the fragmentation very strongly.

List of papers

I E. Kukk, R. Sankari, M. Huttula, S. Mattila, E. Itälä A. Sankari, H. Aksela, S. Aksela: *Dissociation of acetonitrile molecules following resonant core excitations*, International Journal of Mass Spectrometry, **279**, 69 2009. second paper here

II E. Itälä, S. Granroth, D. T. Ha, L. Partanen, A. Caló, H. Aksela, S. Aksela, E. Kukk: *Fragmentation patterns of doubly charged acrylonitrile molecule following carbon core ionization*, Journal of Chemical Physics, **313**, 114314 2009. third paper here

III K. Kooser, D. T. Ha, S. Granroth, E. Itälä, L. Partanen, E. Nõmmiste, H. Aksela, E. Kukk: *Resonant Auger electron-photoion coincidence study of the fragmentation dynamics of an acrylonitrile molecule*, Journal of Physics B, **43**, 235103 2010

IV E. Itälä, D. T. Ha, K. Kooser, E. Rachlew, M. A. Huels, E. Kukk, E: *Fragmentation patterns of core ionized thymine and 5-bromouracil*, Journal of Chemical Physics, **133**, 154316 2010.

V E. Itälä, D. T. Ha, K. Kooser, E. Rachlew, E. Nõmmiste, U. Joost, M. A. Huels, E. Kukk: *Molecular fragmentation of pyrimidine derivatives following site-selective carbon core ionization*, Journal of Electron Spectroscopy and Related Phenomena, **184**, 119 2011.

VI E. Itälä, D. T. Ha, K. Kooser, E. Rachlew, E. Nõmmiste, U. Joost, M. A. Huels, E. Kukk: *Fragmentation patterns of core ionized uracil*, International Journal of Mass Spectrometry, **306**, 82 2011.

VII E. Itälä, D. T. Ha, K. Kooser, E. Rachlew, M. A. Huels, E. Kukk: *Fragmentation patterns of thymidine induced by valence and carbon 1s photoionizations, manuscript submitted to Physical Chemistry Chemicl Physics.*

VIII E. Itälä, K. Kooser, E. Rachlew, M. A. Huels, E. Kukk: *Soft x-ray induced fragmentation of glycine, manuscript.*

Chapter 1

Introduction

The desire for understanding the surrounding world has always been a strong human character. It is therefore no surprise that the idea of all matter consisting of tiny blocks - atoms - has its origins in ancient India and Greece. As for molecules, the concept began to evolve in the 17th century leading to sophisticated quantum mechanical models used to describe molecules and clusters today.

Although our knowledge of molecules has increased extensively during the past decades, we are still far from a complete understanding of the effects that govern the world at the molecular level. In order to get more detailed information about such effects, new experimental and theoretical methods are constantly being developed in addition to those already existing. As the world continuously reminds us, the understanding of something usually requires first destroying it. Same goes for the effects on the molecular scale; the structure and characteristics of a molecule often reveal themselves when the molecule is somehow dismantled.

A powerful tool for investigating atoms, molecules and matter in general is electron spectroscopy. Electron spectroscopy is based on detection of electrons ejected from the target sample ionized by absorption of a photon or charged particles. By measuring the kinetic energies of the emitted electrons, one can extract detailed information about the chemical and electronic structure of the target sample. Another widely used method is ion mass spectroscopy, which provides information about the elemental composition and chemical structure of the sample of interest. By combining electron and ion spectroscopies one is able to investigate the structural changes of matter when irradiated with ionizing radiation. Here the interactions between different molecules (see Fig. 1.1) and ionizing radiation have been studied using UV- and x-ray photons. The samples were irradiated

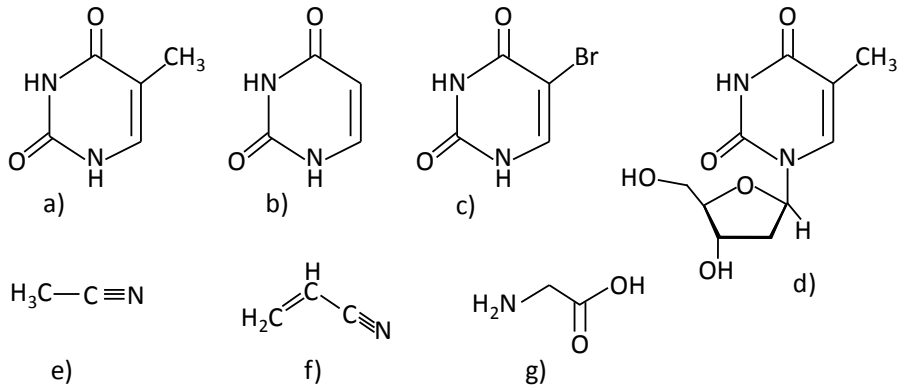

Figure 1.1: Structures of the samples studied here: (a) Thymine $C_5H_5N_2O_2$, (b) uracil $C_4H_4N_2O_2$, (c) 5-bromouracil $C_4H_3BrN_2O_2$, (d) thymidine $C_{10}H_{14}N_2O_5$, (e) acetonitrile C_2H_3N, (f) acrylonitrile C_3H_3N and (f) glycine $C_2H_5NO_2$.

with synchrotron radiation which energy can be tuned freely. This allows probing different inner-shell electronic states and fragmentation processes following different electronic transitions.

Chapter 2

Underlying physics

2.1 Molecules

We picture atoms as spherical hollow constructions with a dense central positively charged nucleus and a cloud of negatively charged electrons orbiting the nucleus at relatively great distances. Molecules are normally considered as simple aggregation of atoms attached to each other by chemical bonds. These chemical bonds are the consequence of a set of atoms seeking the most favorable electronic state in terms of "sharing" a number of electrons [1]. The electrons participating in the bonding process are the outermost valence electrons. Simple molecules can fairly well be described with Lewis structures [2, 3, 4] where bonds are indeed created between atoms by sharing a number of electrons (see Fig. 2.1 (a)). In Lewis model, each electron of a molecule is assigned to a specific atom, which in practice is not the case. A more precise way to describe electrons in a molecule is the molecular orbital (MO) theory [3] which describes electrons as delocalized spreading over the molecule as in Fig. 2.1 (b).

There are many descriptions of the molecular orbital theory in literature [3, 5, 4, 6]; here only a simple introduction is given. Robert Mulliken described molecular orbitals at his Nobel lecture in 1966 in the following way: "Each orbital favors some particular regions of space and disfavors others, yet all the orbitals in a given atom or molecule extend at least to some small extent throughout all regions of the atom or molecule"[7]. In other words, molecular orbital theory considers electrons to belong to the whole molecule; the electrons are distributed across the molecule so that it is possible to calculate the probability to find the electron at any point in

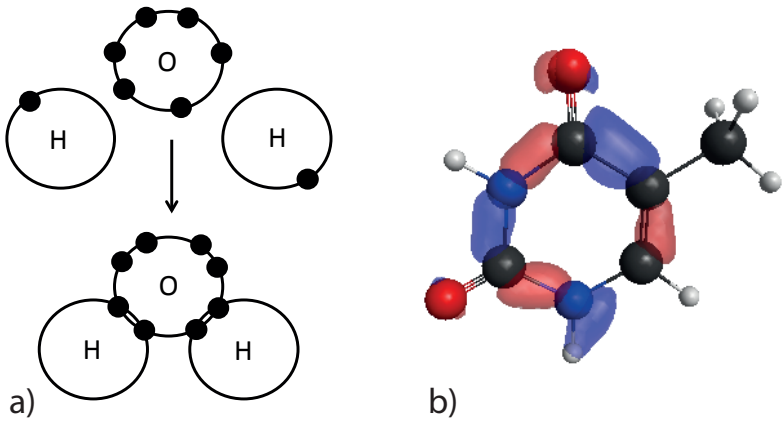

Figure 2.1: In Lewis model, the bonds between two atoms consists of shared electrons (a). In MO theory, the concept of a bond is somewhat vague, the electrons do not belong to any specific atom.

the molecule using the Schrödinger equation:

$$E\Psi = \hat{H}\Psi. \tag{2.1}$$

where E is the energy of the system, Ψ is the wave function of the system and $\hat{H}$ is the Hamiltonian operator.

The Schrödinger equation describing a molecular orbital can be constructed from linear superpositions of atomic orbitals centered on individual atoms (linear combination of atomic orbitals (LCAO) approximation [4, 8, 9]):

$$\Psi = \sum_i a_i \phi_i, \tag{2.2}$$

Where Ψ is the molecular orbital, a_i are mixing coefficients which describe the weights of the contributions of the atomic orbitals to the molecular orbital and ϕ_i are atomic orbitals. In its simplest form, a molecular orbital may be constructed by a sum of orbitals from different atoms.

The physical meaning of the Eq. 2.2 is that when atoms attach to each other forming a molecule, the atomic orbitals start to interact and form molecular orbitals extending over the molecule. By combining atomic or-

bitals, new molecular orbitals are generated. The molecular orbitals are either bonding or antibonding in nature, so one can say that the traditional Lewis model bonds are replaced by molecular orbitals trying to keep the molecule together (bonding) or to break it (antibonding). A molecular orbital is created when two (or more) atomic orbitals with compatibel symmetries overlap and merge. The nature of the MO depends on the signs of the overlapping atomic orbitals; two atomic orbitals with similar signs produce a bonding MO whereas opposite signs produce an antibonding MO. A lack of interaction between atomic orbitals due to the incompatible symmetries results into nonbonding MOs.

Because each molecular orbital is a combination of atomic orbitals, each molecular orbital always resembles certain atomic orbital to some extent(the a_i factor in Eq. 2.2 describes this resemblance). A basic rule is that the core orbitals of atoms in a molecule interact very weakly whereas the outer orbitals interact strongly. So, as the inner molecular orbitals are always almost purely atomic like orbitals and thus localized, the outer orbitals in molecules usually lack the atomic characteristics almost completely.

So there are actually no interatomic bonds that can be cut by removing a specific electron. However the concept of a traditional bond is still very convenient in the description of the fragmentation processes, which are the main topics of this thesis.

2.2 Photon-electron interactions

2.2.1 Photoelectric effect

Perhaps the most widely known photon-electron interaction process is the photoelectric effect, also known as photoionization. First discovered by Heinrich Hertz in 1887 [10], the photoelectric effect was further studied by Philipp Lenard who built an apparatus capable of measuring the velocity of the electrons emitted from a metal surface by UV light [11]. Finally explained mathematically by Einstein in 1905 [12], the photoelectric effect (see Fig. 2.2) is a process where a photon with sufficient amount of energy (hv) gets absorbed by an electron in an atom or a molecule causing the electron to be ejected from the atom or molecule (see Fig. 2.2):

$$M + hv \longrightarrow M^+ + e^-. \tag{2.3}$$

The energetics of the photoionization is defined by the Einstein equation, which is an example of the conservation of energy:

$$K.E. = hv - I, \tag{2.4}$$

where $K.E.$ is the kinetic energy of the electron absorbing the photon and I is the ionization or binding energy of the electron involved [13, 14]. Normally, in an atom or molecule, there are numerous electrons with different binding energies. Thus, if the energy of the ionizing radiation is constant, the energy distribution of the photoelectrons produce an energy spectrum characteristic of the target atom or molecule.

2.2.2 Photoexcitation

An atom or a molecule in a neutral state where the electrons populate the lowest possible orbitals and the system is said to be in its ground state. In addition to the occupied orbitals, atoms and molecules also have a large number of unoccupied orbitals. If an atom or a molecule absorbs a photon with specific energy, one of these orbitals may become populated and the atom or molecule becomes excited [13, 15]. The process

$$M + hv \longrightarrow M^* \tag{2.5}$$

is called photoexcitation or resonant excitation (see Fig. 2.2). It is possible only when the photon energy hv fulfills the condition

$$hv = E_e - E_v, \tag{2.6}$$

where E_e and E_v are the binding energies of the orbitals where the electron is promoted from and excited to respectively. In general, excitations where electrons are promoted from the core orbitals result in a much more unstable state compared to the promotion of a valence electron.

2.2.3 Auger process

Now we know that a photon with a suitable energy can remove or promote a core electron in an atom or molecule. This core hole state is highly excited and unstable leading to de-excitation process. De-excitation is simply a process where the excited electronic structure rearranges to an energetically lower, more stable state via radiative (fluorescence, not discussed here) or

non-radiative processes. When dealing with light elements the non radiative Auger decay processes are the dominant ones [8, 16]. In Auger decay, the core hole is filled with an electron from a higher orbital and simultaneously another electron is emitted as presented in Fig. 2.2. Auger decay can be the result of core ionization leading to a doubly ionized state

$$M^{+} \longrightarrow M^{++} + e_A, \tag{2.7}$$

a process called as normal Auger, or core excitation leading to a singly ionized state

$$M^{*} \longrightarrow M^{+} + e_A, \tag{2.8}$$

namely as resonant Auger. The kinetic energy for the Auger electron is

$$K.E._{Auger} = E_c - E_{v1} - E_{v2}, \tag{2.9}$$

where $K.E._{Auger}$ is the kinetic energy of the ejected electron, E_c is the binding energy of the core hole to be filled, and E_{v1} and E_{v2} are the binding energies of the orbitals where the final state holes are located. This is a rather crude approximation, as it does not take into account electron relaxation involved in the norma Auger process.

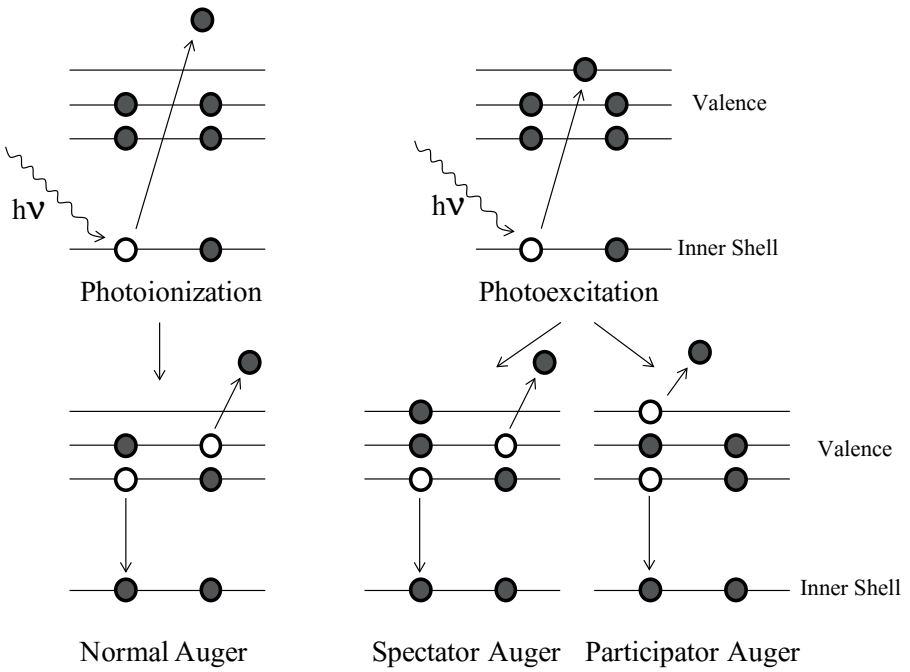

Figure 2.2: Photoabsorption and the following non-radiative decay processes.

Chapter 3

Experimental methods

3.1 Synchrotron radiation

When the velocity of a moving charged particle changes, electromagnetic radiation is created[17]. Radiation emitted by a charged particle moving along a circular path with relativistic velocity is generally called synchrotron radiation. The name originates from the discovery of synchrotron radiation which was first observed in 1946 in a General Electric synchrotron accelerator [18]. Originally synchrotron radiation was considered to be a disadvantage related to operation of elementary particle accelerators, but during 1950s and 1960s it became clear that synchrotron radiation could also be a beneficial tool for practical applications [19]. Nowadays synchrotron radiation is widely used for example in the fields of physics, chemistry, engineering and life sciences. Synchrotron radiation and its characteristics are discussed here on a more general level, but there can be found numerous description of synchrotron radiation in literature, -some of which are very detailed [20, 21, 22].

In a modern synchrotron, the synchrotron radiation is emitted by electrons traveling in a circular path with relativistic velocity. A schematic of a synchrotron is shown in Fig. 3.1. The high-velocity electron current is achieved by first injecting the electrons to the storage ring with an electron gun or a similar device. Once the electrons are in the storage ring, they are accelerated to their final velocity by "pumping" kinetic energy to them using radio frequency (RF) cavity. After each cycle of the acceleration the magnetic field strength of each bending magnet is increased in order to maintain the electrons in correct trajectories. Each time an electron moves on a circular path, synchrotron radiation is created and the electron looses a fraction of its energy. This energy loss is compensated by boosting the

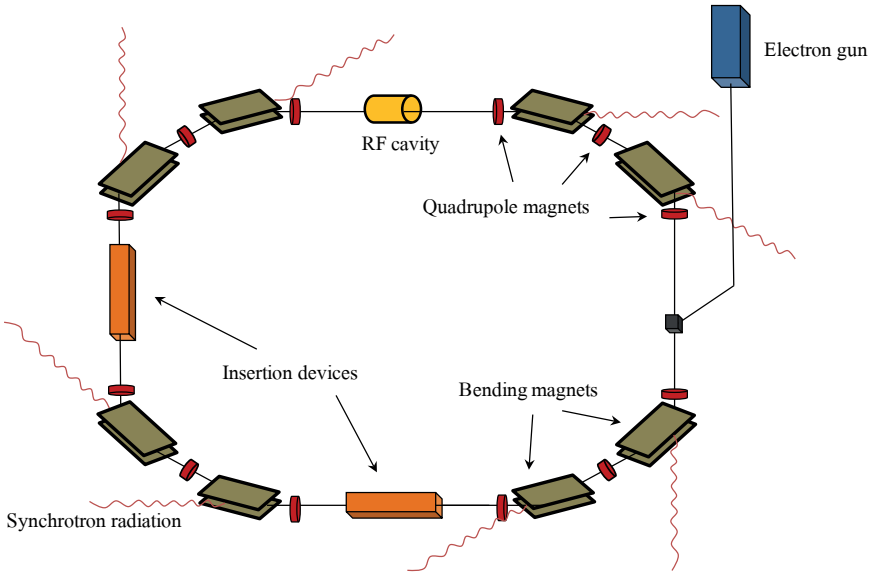

Figure 3.1: Schematic of a synchrotron.

electron kinetic energies in the RF cavity. In addition to bending magnets, different quadrupole magnets along the storage ring also help the electrons to maintain the desired trajectory instead of diverging and hitting the storage ring walls.

Synchrotrons are often equipped with so called insertion devices are needed, which provide much more intense radiation than bending magnets alone. A typical insertion device consists of an array of magnets which force the electron to oscillate rapidly instead of moving along a straight trajectory. These oscillations that are generated in the straight sections of the ring, create synchrotron radiation that has characteristics far superior than the bending magnet radiation.

3.1.1 Characteristics

Synchrotron radiation has many properties that make it a superior tool for probing different processes that occur at the atomic or the molecular level. Unlike traditional x-ray tubes or gas discharge lamps, synchrotron provides radiation with continuous energy spectrum and several orders of

magnitude higher the brightness and energy. This is important because many experiments, like the ones related to this thesis, use small samples that can use only a tiny fraction of the emitted radiation. A charged particle moving through a bending magnet with relativistic velocity emits radiation with power

$$P = \frac{e^2 \gamma^4 c}{6\pi\varepsilon R^2}, \tag{3.1}$$

where e is the electron charge, c is the speed of light, ε is the permittivity of free space and R is the radius of motion. The relativistic parameter $\gamma = E/m_0 c$, where E is the electron energy and m_0 its rest mass [20, 25]. A more practical expression for the total radiated power of a storage ring can be expressed as a function of the electron current I:

$$P_{tot} = \frac{88.5 E^4 I}{R}, \tag{3.2}$$

where P is in kW, E in GeV, I in A and R in m. Compared to a traditional high-energy x-ray tube, the power of bending magnet radiation is over 1000 times higher [23]. Synchrotron radiation is emitted from a bending magnet in a narrow cone (see Fig. 3.2) producing a continuous spectrum that covers all wavelengths from infrared to hard x-ray region as in Fig. 3.3. These two characteristics are a direct consequence of the relativistic velocity of the radiation emitting particles [20].

Nowadays maybe the most common source of synchrotron radiation are undulators (see Fig. 3.3) which provide even several orders of magnitude brighter radiation than bending magnets. Electrons moving through an undulator oscillate with amplitudes small enough for the electromagnetic waves emitted by each undulation to be coherent and to sum up; interference between the electromagnetic waves takes place.

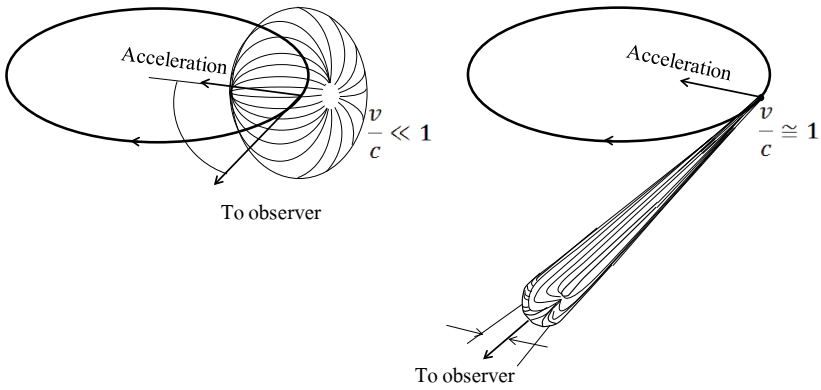

Figure 3.2: Electromagnetic radiation as the observer sees it in the case of a charged particle moving along a circular trajectory with non-relativistic (a) and relativistic (b) velocities.

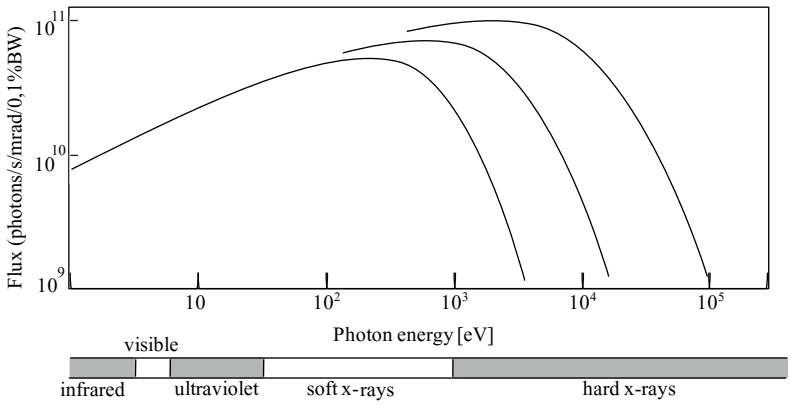

Figure 3.3: Synchrotron radiation originating from bending magnets has a wide spectrum with high intensity.

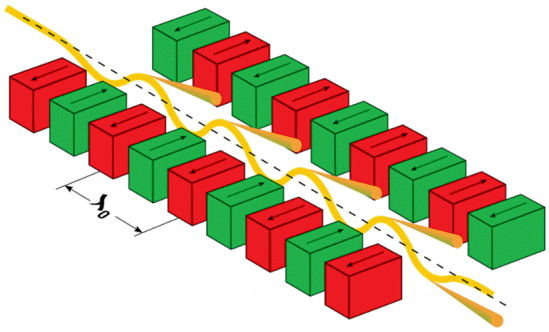

Figure 3.4: Schematic of an undulator; the electrons traveling through an array of magnets emit very intense radiation in narrow energy bands [24].

Due to the interference, undulator radiation is highly collimated, has high flux per solid angle and high brilliance. Interference also causes the energy spectrum of an undulator not to be continuous but a sequence of sharp peaks. Energies of these interference maxima are given by the so called *undulator equation*

$$h\nu_n = n\frac{2hc\gamma^2}{\lambda_0}(1 + \frac{K^2}{2} + \gamma^2\theta^2)^{-1}, \qquad n = 1, 2, 3..., \tag{3.3}$$

where θ is the emission angle with respect to undulator axis, λ_0 is the period of the magnetic array and K is a dimensionless undulator parameter. K is defined so that K/γ is the maximum angular deviation of the electron trajectory in the undulator. One can easily notice from the equation (3.3) that the radiation energy of an undulator can be adjusted by changing the K parameter [20]. In practice this is done by changing the gap between the magnet arrays. Figure 3.5 illustrates the undulator energy distribution at beamline I-411 at MAX II storage ring.

3.1.2 Beamline I-411

All the experiments related to this thesis were conducted at beamline I-411 which is located at 1.5 GeV Max II storage ring, Lund, Sweden. The

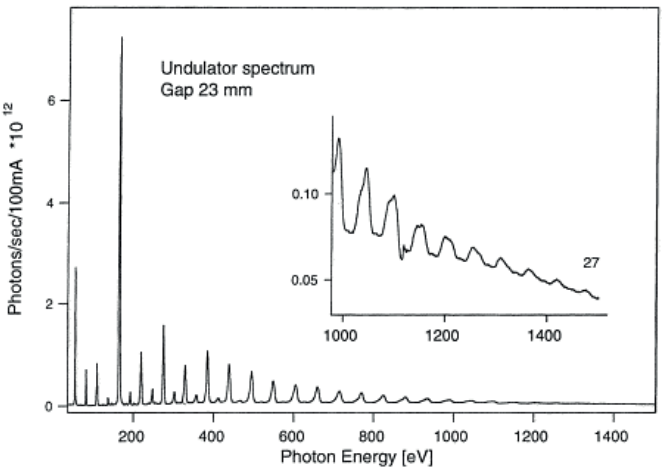

Figure 3.5: Energy spectrum of an undulator consists of intensive narrow peaks. This spectrum is from an undulator located at beamline I-411 at MAX-II storge ring [26].

beamline is based on a 2.65 m long hybrid undulator [27] with 88 poles which produces a high flux of photons from 50 to 1500 eV. The photon flux on sample is $10^{11} - 10^{13}$ $photons/s$ and the resolution E/dE is $10^3 - 10^4$ depending on the photon energy. The synchrotron light is conducted into the experimental end station through a set of mirrors, a plane grating and a SX700 monochromator which define the energy resolution. The beamline is pictured in Figure 3.6; before the experimental end station there is a one meter long section of the beamline available for the installation of different setups, such as the electron-ion coincidence setup related to this thesis, can be installed.

The radiation from the undulator is first conducted through water cooled mirrors (M1) and (M2) and plane grating where most of the heat load of the radiation is absorbed. The monochromator provides the beamline with high resolution suitable for different high quality emission and absorption spectroscopy measurements. The final vertical and horizontal focusing onto the end station is achieved with a toroidal refocusing mirror (M4). A differential pumping stage of about one meter length separates a pressure difference of five orders of magnitude between the end station and the beam line without the use of windows. This is the key feature for the ability to

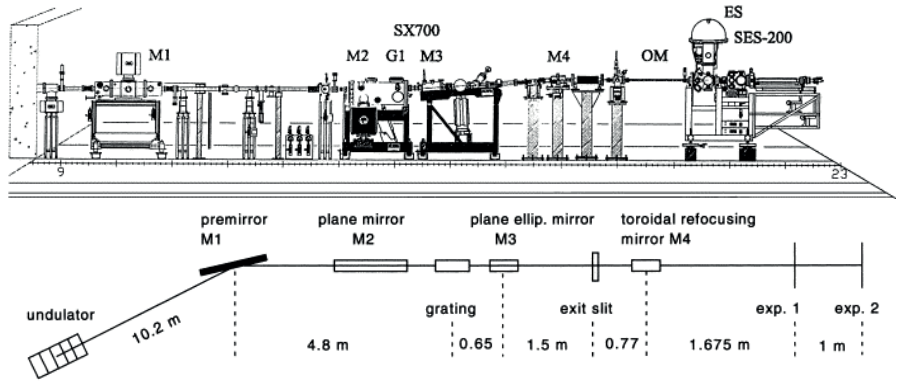

Figure 3.6: Schematic of a beamline I-411 located at MAX-II storage ring [26, 28].

perform gas phase experiments without detrimental effects on the ultrahigh vacuum in the rest of the beamline.

3.2 Spectroscopic methods

This work was carried out applying an experimental method called Photo-Electron-PhotoIon(-PhotoIon) coincidence (PEPI(PI)CO) spectroscopy. As the name already implies, the method combines electron- and ion spectroscopy.

3.2.1 Electron spectroscopy

Electron spectroscopy utilizes the electron spectrometer, which is an apparatus used to analyze the kinetic energy distributions of electrons emitted from solid, gaseous or even liquid samples as a result of particle or photon bombardment. The kinetic energy distribution of the photoelectrons displays molecular (or atomic) electronic energy levels *i.e.* binding energy of the electrons. In the case of double ionization, core ionization takes place; the energy spectrum shows well resolved photolines with high binding energy (Fig. 3.7). Single ionization on the other hand involves electron ejection from one of the valence orbitals. In a valence electron energy spectrum the photolines are not so well resolved (see Fig. 3.8) and the binding

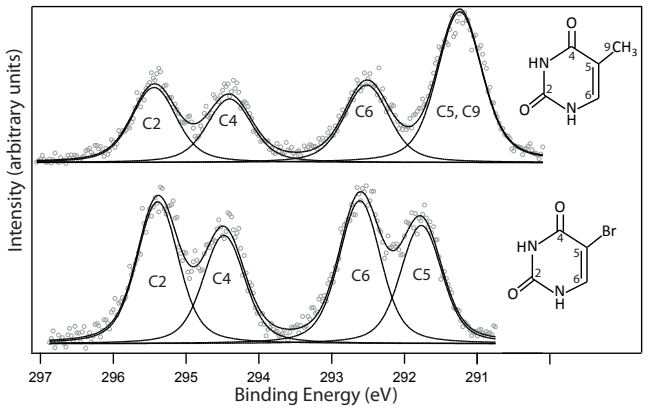

Figure 3.7: C 1s electron spectra of thymine (upper) and 5-bromouracil (lower). Each carbon atom is located in a different chemical environment which results into chemical shifts of different magnitudes.

energy corresponding to the photolines is around ten eV. In valence region there are often many molecular orbitals separated by a fraction of an eV [29], which causes the photolines of the electron spectrum to be broad.

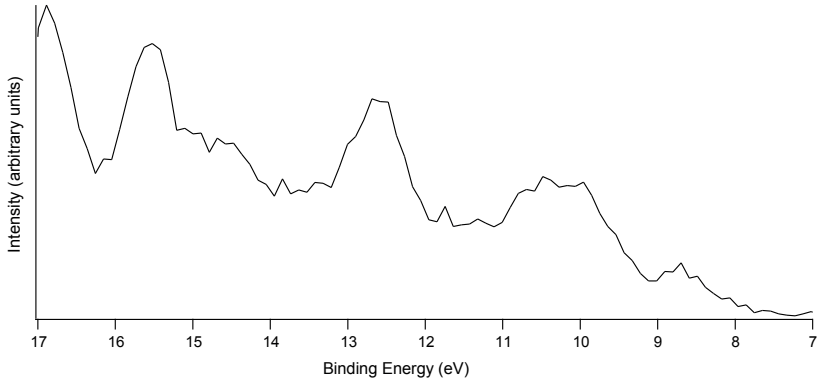

Figure 3.8: An electron spectrum of thymidine representing the binding energies of the electron in the outermost molecular valence orbitals.

The binding energy of a core electron in an atom depends strongly on

the atom's chemical environment; *e.g.* the binding energy for a carbon 1s electron in solid state graphite is 284.5 eV [30] whereas the binding energy of C 1s electron in gaseous CO_2 is 297,7 eV [31]. This kind of change of binding energy when the chemical environment changes, is called "chemical shift". The chemical shift is perhaps better described with a molecule with several atoms of the same element in different chemical environments, such as the thymine and 5-bromouracil molecules in Fig. 3.7. The simplest explanation of chemical shifting is based upon the electronegativity of the neighboring atoms. Electronegativity describes the tendency of an atom to attract electrons, thus when two unlike atoms are bonded, the core level binding energies of the atom with lower electronegativity became shifted towards higher binding energy. Thymine and 5-bromouracil consist of C, H, N and O atoms (and of an Br atom in the case of 5-bromouracil), out of which the O is the most electronegative one before N. As the Figure 3.7 shows, the electrons belonging to carbons neighboring an oxygen atom, are drawn more to the higher binding energy than those neighboring a nitrogen atom. Furthermore, as the 5-bromouracil's only difference from thymine is that in 5-bromouracil the methyl group is replaced with Br, the C 1s spectra of the two molecules are almost identical. The only difference is that the electrons of to the C5 carbon of 5-bromouracil have shifted to slightly higher binding energy. This is due to the larger electronegativity of Br over carbon.

The origins of electron spectroscopy dates to 1887 when Heinrich Hertz first observed the photoelectric effect, but it was the invention of the X-ray photoelectron spectroscopy (XPS) by Kai Siegbahn in 1957 [32] that really made electron spectroscopy what it is today; one of the most important tool for investigating chemical composition of matter. The most common electron spectrometer type nowadays is a hemispherical design. Its main components are (see Fig 3.9) a hemispherical energy analyzer and a lens system that is used to lead the electrons from the target to the hemisphere. As the name implies, the working principle of a hemispherical electron analyzer is based on the electric field created between two half-spheres with a common center. The energy discrimination is based on the Lorenzian force which states that a charged particle moving in a magnetic ($\vec{B}$) and electric (E) field is subjected to a force

$$\vec{F} = q(E + \vec{v} \times \vec{B}), \tag{3.4}$$

where q is the particle's charge and $\vec{v}$ is its velocity.

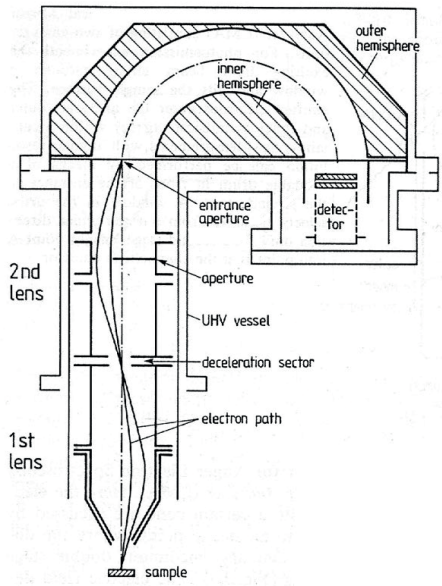

Figure 3.9: Schematic of an electron spectrometer. The major differences between the electron spectrometer of the Figure and the one used here is that the applied spectrometer has a seven element lens system and no exit slit.

The electric field between the two hemispheres is set so, that only electrons with specific energy, the pass energy, can reach the detector. The pass energy (E_{pass}) together with the entrance slit (and the exit slit, depending on the spectrometer design) width determines the resolution of the spectrometer. A good estimation for the spectrometer's resolution is

$$\triangle E = \frac{w}{2R} E_{pass}, \tag{3.5}$$

where w is the entrance slit width and R is the radius of the orbit of an electron with kinetic energy equal to the E_{pass}.

The electrons emitted from the sample are collected and conducted to the energy analyzer by a retardation lens system. The system consists of

several electric lenses, which decelerate and accelerate the collected electrons to match the pass energy of the analyzer. Only electrons emitted with specific energy can get trough the lens system and enter the analyzer. An entire spectrum is thus recorded by scanning the voltages of the electric lenses over a range that covers the required electron energies. Unlike the spectrometer in Fig. 3.9, the modified SES-100 electron spectrometer used here has a seven-element retardation lens system. The electron detector is a positive sensitive resistive anode (Quantar Model 3394A) with a Quantar Model 2401B Position Analyzer ADC unit [33, 34]. The data is collected with a special self-made computer program.

3.2.2 Ion spectroscopy

In ion spectroscopy the positive charged particles produced by ionization are collected and analyzed. In this work, the so called ion time of flight (TOF) spectrometer, which measures the flight times of the detected ions, is used. A commonly used TOF spectrometer is a Wiley-Mclaren type linear design described [35] in Figure 3.10. The main characteristics of a Wiley-Mclaren TOF are high transmission with high sensitivity, fast analysis speed and the easiness of the mass scale calibration. The upper limit for the mass scale, which in principle does not exist, is practically in the range of kDa.

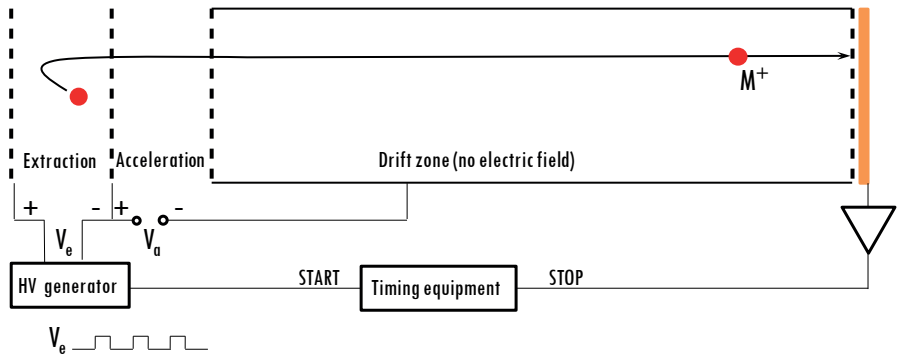

Figure 3.10: Schematic of a linear Wiley-McLaren type time of flight spectrometer.

The ions are created in the sample or extraction region of the spectrometer where the ions are subjected to an electric field forcing them towards the detector. When the ions leave the sample area, they enter the acceleration area where all the ions are accelerated with constant electric field to a specific kinetic energy. After the acceleration area, the ions enter the long field free drift zone after which they hit the detector. The extraction voltage V_e is often applied in short pulses that push the ions off the samples area where they have been gathered between the pulses. These pulses also serve as the starting signal of the ion time of flight monitoring, which stops when the ion hits the detector (see Fig. 3.10). The flight time dispersion relies on the fact that all the ions receive the same amount of kinetic energy in the acceleration region so that the flight time is then proportional to the ion's mass to charge M/q ratio:

$$T = T_0 + C\sqrt{\frac{M}{q}}, \tag{3.6}$$

where T_0 and C are constants depending on the spectrometers geometry and the applied electric fields.

Several methods to convert the ion flight times into M/q scale exist, but one easy and accurate way is to use well known mass peaks. In a vacuum chamber with pressure of around 10^{-7} mbar, there are always always residual gases present, namely H_2O, N_2 and O_2. Using the flight time peaks of these gases, it is easy to derive the T_0 and C of the eq. 3.6 and thus convert the TOF scale into M/q scale.

3.2.3 Coincidence techniques

Although energy resolved electron and ion spectroscopic techniques alone provide valuable information about the relaxation [36, 37] and fragmentation [38, 39] processes following ionization or excitation, different coincident techniques offer possibilities for much more complete and detailed determination of different decay channels of ionized and excited atoms and molecules[40, 41, 42, 43]. Different coincident techniques and designs exist depending on what kind of processes one wishes to monitor (see Fig. 3.11); here the main focus is on sequential fragmentation processes, so a suitable coincidence setup is the so called PhotoElectron-PhotoIon-PhotoIon coincidence (PEPIPICO) technique [44, 45, 46, 47]. In Fig 3.11 there is a sketch

with time scale of those processes following an absorption of a high energy photon. The highly excited states such as core hole states, decay normally

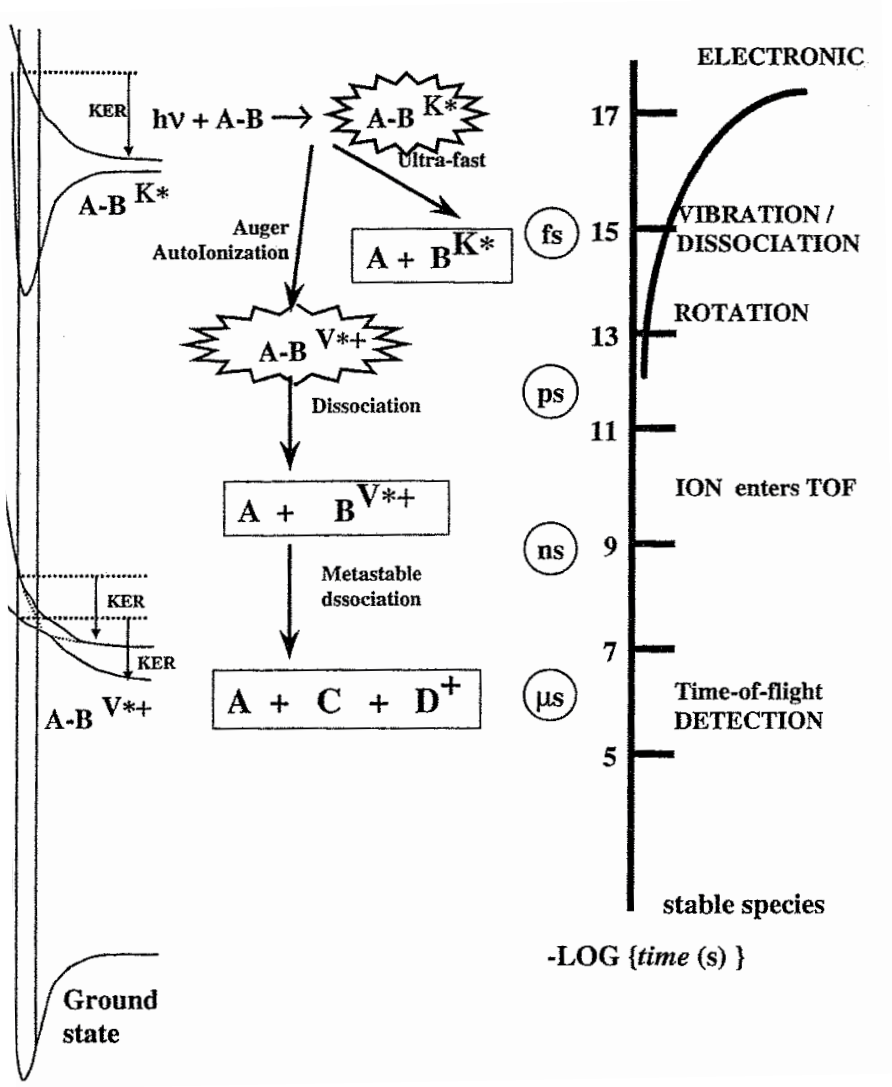

Figure 3.11: Events and time scales for core level photoionization. K^* indicates core excited state and V^{*+} refers to a valence excited ion[48].

in a femtosecond time scale. Furthermore, the relaxation of a core hole state most likely leads to a multiply charged state which often is unstable and fragments by charge separation.

One of the main goals when studying inner shell photoionization dynamics is to increase the understanding of electronic relaxation processes resulting to bond-breaking and in particular the sequence of events in multistep decay processes. In order to obtain such information, coincident techniques that detect most, if not all, particles produced in an ionization or excitation process are needed. To study the sequence of bond-breaking processes following core ionization, it is reasonable to monitor photoelectrons in coincidence with the photoions. However, if the wish is to also determine the electronic states leading to different fragmentation channels, it is better to monitor Auger electrons instead of the photoelectrons in coincidence with the photoions, or furthermore both photoelectrons and Auger electrons in coincidence with the photoions.

The problem with this kind of setup is that as photoelectron-photoion coincidence measurements are quite time consuming themselves, coincidence measurements with Auger electrons are even more time consuming. Furthermore, if one wishes to monitor multiple electrons originating from a single ionization/excitation event, the technical challenges become substantial.

PEPIPICO technique and apparatus

As mentioned earlier in this chapter, the experimental technique used in this thesis is the so called PEPICO or PEPIPICO technique, depending on whether one or multiple ions wae measured in coincidence with one photoelectron. The idea of the technique is to detect a photoelectron and the corresponding photoion(s) originating from a single ionization event. PEPI(PI)CO technique has its origins in the 1960s when K. E. McCulloch and his co-workers first observed directly the decomposition of multiply charged ions into singly charged fragments [49]. Since their pioneering work, many groups around the world have successfully applied PEPI(PI)CO techniques in various studies [40, 50, 51, 52, 53].

The principle of PEPI(PI)CO is to measure ions that are created following a specific ionization process *e*.g. C 1s core ionization. Such ions are those detected in coincidence with energy-selected electrons [54, 55]. The electron energy can be selected freely and due to the modern syn-

chrotron facilities, possibilities for specific electron transition monitoring are nearly countless. Thus the PEPI(PI)CO technique is a very useful tool for studying different processes governing the interaction between matter and ionizing or exciting radiation. Here the main focus has been on fragmentation dynamics of doubly ionized molecules into pairs of cations, hence PEPIPICO technique has mainly been used. In addition to determining the fragmentation pathways of the sample molecules, also the effects of geometry, initial ionization site and (to some extent) chemical environment has been studied.

The experimental setup schematics is presented in Fig. 3.12. The

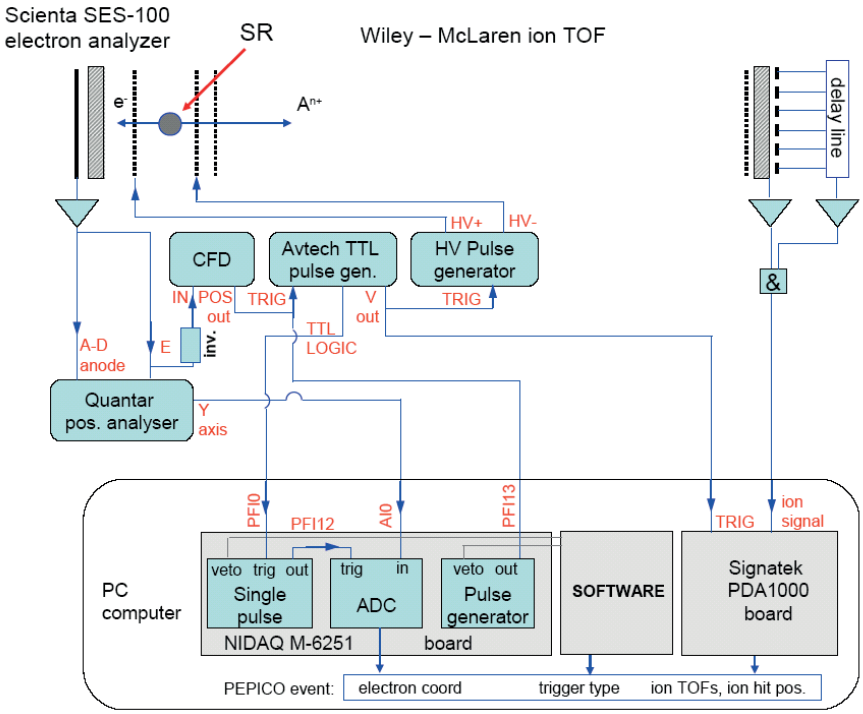

Figure 3.12: Schematic of the electronic components in the PEPIPICO equipment used here. The delay line has not been connected in the present study.

apparatus consists of a modified Scienta SES-100 electron energy analyzer

[34], where the original CCD camera was replaced by a resistive anode detector (Quantar), and a home-made Wiley-Mclaren type ion time-of-flight spectrometer with a 400 mm long ion drift tube. The ion spectrometer is equipped with a 77 mm Hamamatsu MCP detector with the anode consisting of 10 concentric rings. The ion TOF is determined by the recharge signal pulse from the MCP stack and the pulses from the anode rings are delayed by 50-100 ns with 5 ns steps. These can be used to determine the radial hit distance from the instrument's axis, which in turn can be used to determine the initial velocity vector of the detected ion (this has not been used here). The ion detection electronics is based on a 1 GHz waveform digitizer card (Signatec PDA 1000). For the PEPIPICO measurements, the PEPICO system is operated in the pulsed extraction field mode. The ion extraction pulses were triggered by the fast preamplifier signal from the electron detector. The samples were evaporated into the interaction area using an effusion cell with integrated cooling shroud (MBE Komponenten NTEZ40 oven).

In a coincidence measurement an electron arriving to the electron analyzer creates a signal which is used to start the ion flight time measurement. The signal triggered by the electron is first detected by the Quantar position analyzer, which sends a signal to the Avtech pulse generator which sends a signal to the HV pulse generator and to the Signatek PDA 1000 digitizer card. So, as the HV pulse generator turns the extraction voltages on, the signal to the digitizer card starts the flight time monitoring. The stop signal for the flight time is generated when the ion(s) hit the MCP. The flight time monitoring does not stop when the first ion hits the detector. Instead, after the start signal there is a certain time interval (for example $20\mu s$), during which the flight times of all the ions arriving to the detector are recorded. The extraction voltages are kept on during the flight time monitoring, so the possible new start signals trying to turn on the extraction voltages and start the flight time monitoring during the already ongoing flight time monitoring have no effect.

Chapter 4

Electron-Ion-Ion coincidence data analysis

In this chapter we discuss how the PEPIPICO data are presented, what kind of information can be extracted from such data and how it is done. We begin by shortly describing the ion fragments' trajectories from the interaction region of the measurement equipment to the detector and thus justifying the applied data handling procedure. Finally different fragmentation processes are discussed.

Core hole states usually lead to fragmentation processes, where large amount of kinetic energy is released. This is due to the Coulombic repulsion which causes the charged ion fragments to have notable axial velocity before they are extracted from the source region, accelerated and conducted to the detector. Therefore the flight times of the ions are altered and the flight time (and the mass) peaks in the spectrum are broadened, which is quite a nuisance. This disadvantage can, however, be turned into advantage. This is because instead of being a continuous measurement, a PEPIPICO measurement is a dataset that consists of a large number of recorded events, that include an electron detection and a number of ion flight time detections that correspond to ions originating from the same ionization event as the electron. A great benefit of this kind of dataset is that one can express it as a two dimensional (faster coincident ion vs. slower coincident ion) plot, where each coincident ion pair appears as tilted patterns. Figure 4.1 displays such plot, also called as PEPIPICO map.

The pattern formation is explained by the dissociation dynamics: the Coulombic repulsion forces the ion fragments to eject to opposite directions with notable axial velocity when separating (see Fig 4.2). Because the ion

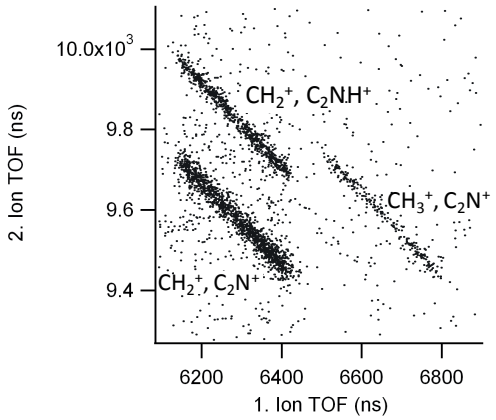

Figure 4.1: In a PEPIPIO map the coincident fragments appear as tilted patterns. The center coordinates of the pattern corresponds to the nominal flight times of the ion fragments. The parent molecule here is acrylonitrile C_3H_3N.

fragments are eventually all collected to the detector, the initial axial velocity only increases or decreases the flight times of the ions. If the ejection direction of the ion fragments is considered to be isotropic, then after detecting enough of those fragments originating from one kind of dissociation event, the 2D ion-ion plot looks like a cigar-shaped pattern as in Fig. 4.1.

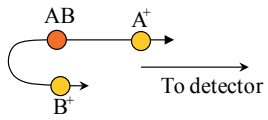

Figure 4.2: The kinetic energy released in the charge separation forces the coincident ion fragments to opposite directions. Although the lighter fragment reaches the detector first, each fragment will have a spread in flight time $\triangle$T due to the different trajectories.

These patterns tell many things about the fragmentation, *e.g.*, how much kinetic energy is released during the process or how the fragmentation

process proceeds step by step. However, before going into a more detailed pattern analysis, an introduction to different fragmentation processes of doubly ionized molecules is given.

4.1 Fragmentation mechanisms

As already mentioned in the previous section, core ionized molecules have a strong tendency to relax into doubly valence-ionized states. These states, in turn, are unstable and fragment most commonly into pairs of cations via charge separation. The fragmentation is preceded by geometrical changes during which the positive charges localize to certain fractions of the doubly charged parent ion. When the dissociation comes to a certain point, the charge separation induced by Coulombic repulsion between the two positive charges takes place.

4.1.1 Two-body dissociation

Two-body dissociation is the most simple charge separation process where the doubly charged molecule fragments into two singly charged cations. The momentum of the fragmentation is the vector sum of each fragment (which is zero) plus the momentum of rotational, vibrational and thermal movement of the parent molecule. In practice, the momentum of the fragmentation governed by the electrostatic repulsion between the similarly charged fragments is much larger than the thermal momentum at room temperature. The momentum conservation law states that the momenta of the two charged fragments are equal, but have opposite directions:

$$m_1 v_1 = -m_2 v_2, \tag{4.1}$$

where m_1 and v_1 are the mass and velocity of the first fragment and m_2 and v_2 are the mass and velocity of the second fragment. The ion flight times are thus anticorrelated.

4.1.2 Many-body dissociation

It is very common that as the parent dication molecule dissociates into pairs of cations, also neutral fragments are ejected. The three-body processes, where only one neutral fragment is ejected, are commonly divided

into three groups [56]:
(1) *Deferred charge separation*, where a neutral fragment is released before the charge separation,
$ABC^{++} \longrightarrow A+BC^{++}$
$BC^{++} \longrightarrow B^{+}+C^{+}$.

(2) *Secondary dissociation,* where the neutral fragment appears after charge separation,
$ABC^{++} \longrightarrow AB^{+}+C^{+}$
$AB^{+} \longrightarrow A+B^{+}$.

(3) *Concerted dissociation,* where the neutral fragment is ejected simultaneously with the charge separation,
$ABC^{++} \longrightarrow A+B^{+}+C^{+}$.

Using the models of three-body dissociations one can easily generate processes producing four or more fragments. Two examples of common four-body processes are:
Secondary decay after the charge separation step, where both charged fragments dissociate further,
$ABCD^{++} \longrightarrow AB^{+} + CD^{+}$.
$AB^{+} \longrightarrow A+B^{+}$ and $CD^{+} \longrightarrow C+D^{+}$.

Deferred charge separation followed by secondary decay,
$ABCD^{++} \longrightarrow A+BCD^{++}$
$BCD^{++} \longrightarrow B^{+} + CD^{+}$.
$CD^{+} \longrightarrow C+D^{+}$.
Figure 4.3 represents one more time the above discussed plus one additional fragmentation processes.

4.2 PEPIPICO pattern slopes

In all of the above processes, a considerable amount of kinetic energy is released, most of it to the singly charged coincident cations. The released kinetic energy is reflected by the length of the pattern, which can be used to determine the released kinetic energy. The equation for deriving the kinetic energy release, however, depends on the fragmentation mechanism. Let us

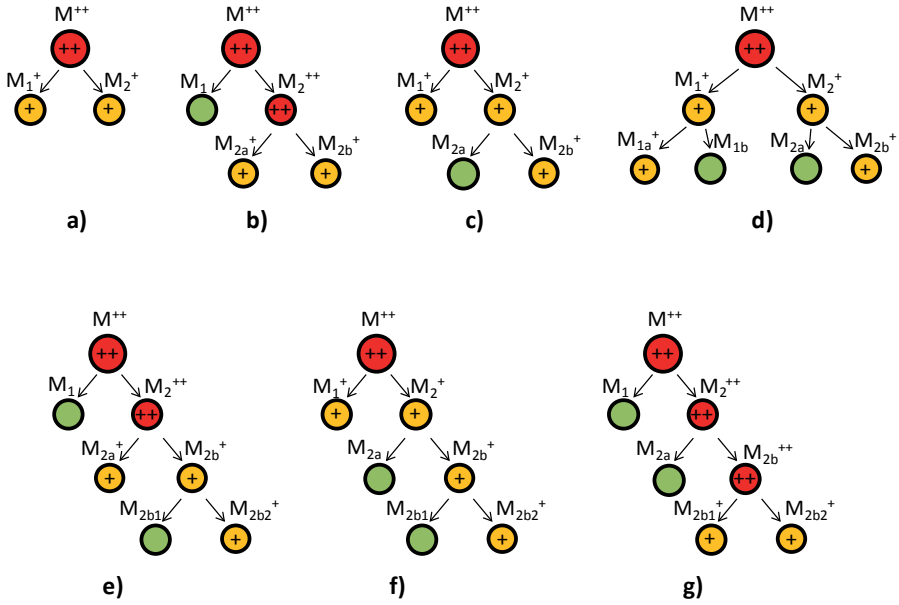

Figure 4.3: There are many different sequential fragmentation mechanisms, which all can be combined using the deferred charge separation and secondary decay.

therefore first define the approximative slope values for different kind of fragmentation processes. The slope value (see Fig. 4.1) is clearly defined by

$$slope = \frac{\triangle T_2}{\triangle T_1}, \tag{4.2}$$

where $\triangle T_1$ and $\triangle T_2$ are the flight time spreads of the faster and slower ion respectively. If we mark the ion's axial velocity in the TOF system as $v_\parallel$, the equations of motion of a charged particle state that in the first approximation the ion's flight time T depends on $v_\parallel$:

$$\frac{\partial T}{\partial v_\parallel} = -\frac{1}{a}, \tag{4.3}$$

where a is the ion's acceleration. The acceleration can be calculated from equation

$$a = \frac{qU}{dm} = C\frac{q}{m}, \qquad (C = constant) \tag{4.4}$$

where q/m is the ion's mass to charge ration and d is the distance- and U is the voltage applied over the sample region of the TOF system.

Now, when the maximum range for the initial axial velocity of the ion is

$$\triangle v_{\parallel} = 2v_{\parallel}, \tag{4.5}$$

we get the corresponding flight time spread:

$$\triangle T = -C\frac{m}{q}2v_{\parallel}. \tag{4.6}$$

When we take the momentum conservation law

$$m_1 v_1 = -m_2 v_2, \tag{4.7}$$

where number 1 and 2 denote the lighter and the heavier fragment respectively, into account, the ion flight times can be written as

$$\triangle T_1 = -C\frac{m_1}{q_1}2v_{1\parallel}, \quad \triangle T_2 = -C\frac{m_2}{q_2}2v_{2\parallel}. \tag{4.8}$$

In a two-body process, where the molecule just fragments into two cations, the slope value is simply

$$\frac{\triangle T_2}{\triangle T_1} = -\frac{q_1}{q_2} \tag{4.9}$$

and if $q_1 = q_2$ we get slope value of -1.

Three-body processes are slightly more complicated; if the fragments are created simultaneously, no general equation for calculating the slope exist. This is due to the fact that although the sum of all momenta must still be zero, the kinetic energy released in the fragmentation may be distributed randomly between all the fragments. For sequential processes, however, it is possible to calculate the slope values. In the case of deferred charge separation the kinetic energy released in the first step is so small that nearly

all the kinetic energy is released in the second, the charge separation step. If we denote the charged fragments produced in the second step as m_{2a} and m_{2b}, the slope equation is

$$\frac{\triangle T_{2a}}{\triangle T_{2b}} = -\frac{q_{2a}}{q_{2b}}, \tag{4.10}$$

as in two-body process.

In secondary decay, the slope value depends on whether the heavier coincident cation is a produced in the first or the second step. Again, the kinetic energy is assumed to mainly go to the charged fragments, so the velocities of the fragments produced in the second step are $v_{2a} \approx v_2$ and $v_{2b} \approx v_2$. The flight time of the ion fragment produced in the second step is thus

$$\triangle T_2 \approx C\frac{m_{2b}}{m_2}\frac{m_1}{q_2}2v_{1\parallel}. \tag{4.11}$$

If m_2 is the cation fragmenting further into m_{2a} neutral fragment and m_{2b} cation and if m_{2b} is heavier than the other coincident cation, the slope is

$$\frac{\triangle T_1}{\triangle T_{2b}} = -\frac{m_{2b}}{m_2}\frac{q_1}{q_2}. \tag{4.12}$$

On the other hand, if M_{2b} is lighter coincident cation, the slope is

$$\frac{\triangle T_1}{\triangle T_{2b}} = -\frac{m_2}{m_{2b}}\frac{q_1}{q_2}. \tag{4.13}$$

In practice, equations 4.12 and 4.13 mean that when m_{2b} is the lighter coincident fragment, the PEPIPICO pattern's slope becomes steeper and vice versa, when m_{2b} is the heavier coincident fragment, the slope becomes less steep.

The deferred charge separation or secondary decay may well also be four-body processes as presented in Fig. 4.2 (e), (f) and (g). Slopes of these processes are determined like was done with processes (b) and (c) of Fig. 4.2. Because in process (e) the kinetic energy is again released mostly to the charged fragments, the slope equation can be written as

$$\frac{\triangle T_{2a}}{\triangle T_{2b_2}} = -\frac{m_{2b}}{m_{2b_2}}\frac{q_1}{q_2} \quad \text{and} \quad \frac{\triangle T_{2a}}{\triangle T_{2b_2}} = -\frac{m_{2b_2}}{m_{2b}}\frac{q_1}{q_2}, \tag{4.14}$$

when m_{2b_2} is the lighter or the heavier fragment respectively. The slope equation for process (f) is exactly the same, only $\triangle T_{2a}$ and m_{2b} of Eq. 4.14 are replaced by $\triangle T_1$ and m_2 respectively. The slope equation for process (g), on the other hand, is similar to the equation of process (b) being $\triangle T_{2b_1} / \triangle T_{2b_2} = -q_{2b_1}/q_{2b_1}$.

Process (d) of Fig. 4.2 where initial charge separation is followed by the ejection of a neutral particle from both singly charged ions ends up having the slope equation of

$$\frac{\triangle T_{1a}}{\triangle T_{2b}} = \frac{m_{2b}}{m_{1a}}\frac{m_1}{m_2}, \text{ if } m_{2b} < m_{1a} \quad \text{and} \quad \frac{\triangle T_{1a}}{\triangle T_{2b}} - \frac{m_{1a}}{m_{2b}}\frac{m_2}{m_1}, \text{ if } m_{2b} > m_{1a}. \tag{4.15}$$

One should remember that all of the above equations apply only if the charged particles ejected isotropically to all directions obtain the major part of the kinetic energy released in the whole fragmentation process.

4.3 Determination of kinetic energy release

As the slope of the PEPIPICO pattern gives information about the fragmentation itself, the length of the pattern gives an estimation about the kinetic energy released in the process. Because the pattern length l is a consequence of a flight time deviation of the ion fragments, the length can be expressed using equations 4.3 and 4.4:

$$l = \sqrt{l_1^2 + l_2^2} = \frac{d\sqrt{8}}{qU}p, \qquad \begin{matrix} l_1 = 2k_1 v_{\|1} \\ l_2 = 2k_2 v_{\|2} \end{matrix} \qquad (k = -\frac{1}{a} = -\frac{dm}{qU}), \tag{4.16}$$

where l_1 and l_2 are the x- an y- axis projection lengths of the pattern (see Fig. 4.4) and p is the momentum of the ion fragments (momentum conservation law: $p_1 = p_2 = p$). Because l is extracted from the PEPIPICO map, the kinetic energy release (KER) can be calculated using momentum conservation law:

$$E_{kin} = \frac{p_1^2}{2m_1} \equiv \frac{p_2^2}{2m_2} \Rightarrow \text{KER} = p^2(\frac{1}{2m_1} + \frac{1}{2m_2}). \tag{4.17}$$

The momentum and KER equations depend on the fragmentation mechanism, which leads to a slightly different presentation for the process pre-

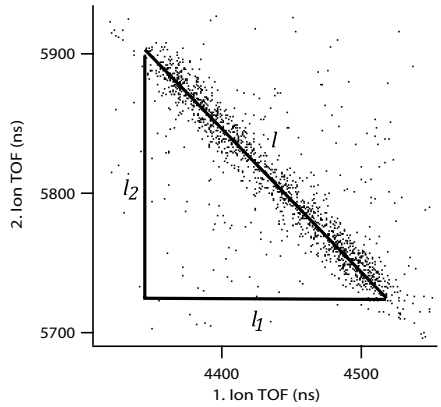

Figure 4.4: A PEPIPICO pattern corresponding to C^+ and CO^+ fragments of CO_2^{++}. The pattern length can be used to determine the KER of the fragmentation process.

sented in Fig. 4.3. In the case of the simplest process, the two-body process (a), the momenta of the ion fragments are equal and the KER value is thus determined by the equation 4.17. In deferred charge separation (process (b)), the momentum correlation is between fragments 2a and 2b. The KER can be determined by equation 4.17, but the masses are now m_{2a} and m_{2b}.

In three-body secondary decay (process (c)), the momentum correlation is between fragments with masses 1 and 2, but the slope length is determined by the fragments 1 and 2b. The momentum of the undetected neutral fragment must therefore be taken into account, so we have

$$p_{2b} \approx \frac{m_{2b}}{m_2} p_2 \Rightarrow l \approx \frac{2d}{qU} \sqrt{1 + \frac{m_{2a}^2}{m_2^2}} \cdot p. \tag{4.18}$$

The KER is still calculated with eq. 4.17, but with using the p value extracted from the equation 4.18. In process (d), the momentum correlation is also between fragments 1 and 2, but here the pattern length is determined

by fragments 1_a and 2_b:

$$l \approx \frac{2d}{qU}\sqrt{\frac{m_{1a}^2}{m_1^2} + \frac{m_{2a}^2}{m_2^2}} \cdot p. \tag{4.19}$$

Again, KER is still calculated with eq. 4.17, but now by using the p value extracted from equation 4.19.

Process (e) is a combination of deferred charge separation and secondary decay, where the momentum correlation is between fragments 2_a and 2_b and the slope length is determined by fragments 2_a and 2_{b2}. The KER is thus determined by replacing m_1 and m_2 in the equation 4.17 with m_{2a} and m_{2b_2} and p by replacing m_{2a} and m_2 of eq. 4.18 by m_{2b_2} and m_{2b}. Momentum correlation is again between fragments 1 and 2 in process (f). The right masses for equation 4.17 are now m_1 and m_{2b_2} whereas for equation 4.18, the right masses are m_{2b_2} and m_2. The last process dealt with here, the process (g), is very similar to process (b). The momentum is distributed between fragments 2_{b1} and 2_{b2}, which are also the fragments determining the slope length. The KER for this kind of process is thus determined with equation 4.17 by replacing m_1 and m_2 with m_{2b_1} and m_{2b_2}.

One should here remember also that the above presented equations are valid or good approximations only when the kinetic energy is mostly distributed between the charged fragments. In other words, the less kinetic energy goes to the neutral fragments, the better the estimation about the KER value is. In processes presented in Figure 4.3, the kinetic energy goes mainly to the charged fragments. In a so called Coulomb explosion, where all the charged and the neutral fragments are formed simultaneously the released kinetic energy can however be distributed between all the fragments, not just between the charged fragments.

Chapter 5

Photofragmentation of molecules

The emphasis of this thesis is on core ionization induced fragmentation which involves the creation of two singly charged ion fragments. However, fragmentation induced by valence ionization and resonant core excitation was also studied to some extent. In the case of core ionization, the fragmentation processes were studied in terms of electron energy resolved PEPIPICO by ionizing C 1s orbitals and measuring the kinetic energies of the C 1s photoelectrons and the flight times of the corresponding coincident photoions. The experimental data was extracted into PEPIPICO maps, which were used to identify the coincident fragments, fragmentation pathways, the intensities of different fragmentation channels and the KER values of the channels using the methods described in chapter 4. Also the role of the initial ionization site and the geometry of the sample in determining the fragmentation pattern was studied together with possible nuclear rearrangements during the fragmentation.

In the case of valence ionization and resonant core excitation only one photoion was formed in coincidence with an electron, thus PEPICO was used. In the case of resonant core excitation the acronym of the method is a bit misleading, the electrons that were monitored in coincidence with the photoions were resonant Auger electrons. The resonant Auger electrons provide information about the electronic final state, unlike the inner shell photoelectrons that provide information about the initial electronic state leading to the detected fragments.

The PEPIPICO maps and the traditional mass spectra that were used to identify the detected ion fragments only provide information about the

masses of the fragments. This can be a problem, because there usually are several different possible fragments with the same mass. In order to reduce ambiguities in identifying the fragments and their sites of origin, isotopic labeling was used. Isotopic labeling means replacing some of the atoms within a molecule with less abundant but sufficiently stable isotopes. Here, some of the isotopic labeling has been used by replacing hydrogens with deuterium atoms or one of the carbons with ^{13}C. For example in the case of acrylonitrile, a sample where all the hydrogens were replaced by deuterium and a sample where the terminal carbon was replaced with ^{13}C were used in addition to the normal sample. Because D and ^{13}C are only one amu heavier than H and C respectively, it is assumed that the isotopic labeling does not significantly alter the fragmentation.

5.1 Photofragmentation of chain compounds

The chain compounds studied here are acetonitrile, acrylonitrile and glycine. The fragmentation of these samples has been studied following core ionization (acrylonitrile, glycine) and resonant core excitation (acetonitrile, acrylonitrile). If one stops to think about fragmentation of a doubly charged molecule into stable fragments, one could easily think that the easiest way (and therefore clearly dominant scenario) would be to cleave one bond to produce two cations. This is a pleasant idea; such a scenario would for example require quite a small amount of energy to take place. However, even with simple molecules such as acrylonitrile, core ionization causes the molecule to fragment via many different channels producing a large number of coincident fragments. The charge separation may take place in the first step or later and the number of final fragments is very often more than two. Fig. 5.1 presents a general picture of fragmentation of doubly charged molecule whereas in Fig. 5.2, three are specific fragmentation pathways of doubly charged acrylonitrile.

When a molecule becomes ionized or excited, it receives additional internal (kinetic and potential) energy which can lead to isomerization *i*.e. nuclear rearrangement of the parent molecule. This was observed with both singly and doubly charged acrylonitrile; there are several fragmentation channels that include hydrogen migration (see *e*.g. Fig 5.2 (c)). Actually, the dissociation processes of ionized molecules can often be considered to begin with geometric rearrangement which is followed by charge separa-

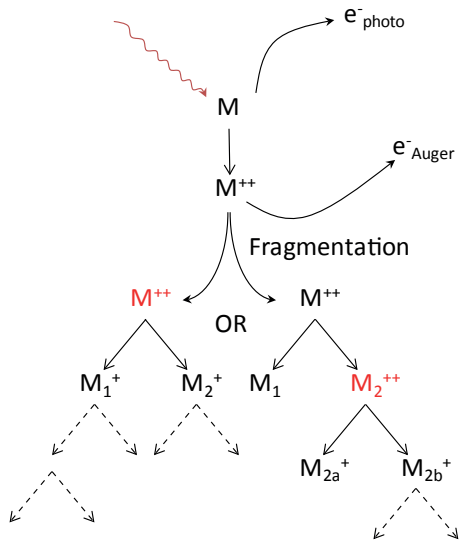

Figure 5.1: Sequence of events induced by core ionization. Core ionization is rapidly followed by Auger decay, which in turn induces the fragmentation of the molecule. The dashed arrows indicate the possibility for further fragmentation.

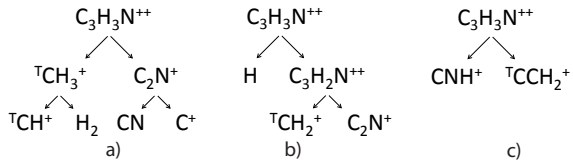

Figure 5.2: Three strong fragmentation channels of doubly charged acrylonitrile. Most commonly the fragmentation pathways of doubly charged acrylonitrile are two step processes. In process (c) a hydrogen has migrated and attached to the nitrogen, before the charge separation and fragmentation takes place.

tion (in the case of doubly charged molecules) and fragmentation. First the molecule starts shifting between different isomers in order to find the most energetically suitable state, overcoming potential barriers. Now, new

bonds are formed and some of the old ones are cut and different fractions of the parent molecule start to move away from each other. Because bond formation depends on interatomic distance, the molecule is considered to be fragmented when the distance between two fractions of the molecule has become too large. In a a model introduced by Eland, during the rearrangement of the molecule, all the fractions of the molecule share the electric charge by rapid exchange (see Fig. 5.3). In other words, the charge(s) jump from one fraction of the molecule to another until the distance between them becomes too large [57]. Due to the Coulombic repulsion, the distances between different fractions of the molecule increase more rapidly in the case of double ionization than in the case of single ionization. The Coulombic repulsion thus acts as an additional dissociative force accelerating the fragmentation process in the case of double ionization.

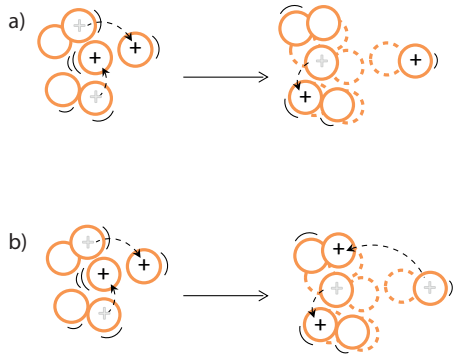

Figure 5.3: Two different fragmentation processes where the other positive charge gets captured in the detaching fragment (a) and where the charge just barely escapes the detaching fragment (b).

The role of the initial core hole on fragmentation was also considered. Based on previous studies concerning site selective fragmentation, especially ionization or excitation of a terminal atom/functional group of a linear molecule, is relatively likely to lead to site selective fragmentation [59, 60, 61]. The general idea here is that the breaking bonds are those next or near the ionized/excited atom. In the case of core ionization of acrylonitrile, the relative intensity changed about 15% when ionizing the terminal carbon compared to the ionization of the other carbons. Also

in the case of core excitation, fragmentation following excitation of core electrons on different atoms resulted into the same fragments with weak changes in relative intensities between the corresponding fragments.

However, fragmentation of acrylonitrile following resonant core excitation depends strongly on the electronic final state (as is the case with acetonitrile also) and thus on the decay process. The resonant Auger decay processes in the case of acrylonitrile (and in the case of acetonitrile) involve electron emission from both outer valence and inner valence orbitals as can be seen from Fig. 5.4. The low binding energy region between 10 and 15

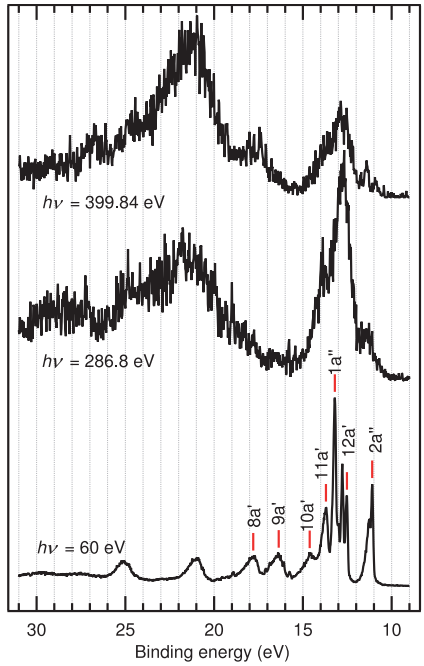

Figure 5.4: Electron spectra of acrylonitrile measured at marked excitation energies [58]. The upper two spectra correspond to the resonant Auger decay after N1s $\rightarrow \pi^*_{C\equiv N}$ $(h\nu = 399,84eV)$ and C1s $\rightarrow \pi^*_{C\equiv N}$ $(h\nu = 286,8eV)$ excitations and the lower corresponds to valence ionization. The valence electron spectrum shows also the configurations of the outer valence hole states.

eV corresponds to participator transitions, whereas the region between 16 and 30 eV is attributed to the different spectator decay channels. In our experiments, participator Auger final states were the only ones producing unfragmented singly charged parent ions. The majority of all the detected fragments, however, resulted from participator Auger final states.

5.2 Photofragmentation of heterocyclic biomolecules

The fragmentation following carbon core ionization of three heterocyclic molecules of biological interest, namely thymine, uracil and 5-bromouracil is studied here. In addition to the experimental research, also some density functional theory (DFT) and unrestricted Hartree-Fock calculations were conducted. The idea of such calculations was to investigate whether the produced fragments could be predicted just by calculating the energy of the possible fragments and their abundancy. This was tested by comparing the experimental intensities of the fragments identified using the slope analysis (as explained in chapter 4) and isotopic labeling with the calculated potential energies of the corresponding fragments. If the most abundant fragments had also had the lowest potential energies, a fragmenting molecule would almost automatically fragment into fragments with the most energetically favorable form. No clear correlation between the calculated energies and the fragment intensities was detected. An apparent explanation of why such simple prediction does not work in case of these, relatively small molecules is that there are usually many potential barriers between the starting geometry of the fragmenting molecule and the energetically most favorable geometries. In case of energy barriers, the molecule has to go through transition states which determine the highest-energy points in the path of geometry changes the molecule needs perform in the dissociation. It is the viewpoint of transition state theory that the energy and character of the transition states determine the transition rates and intensities to various dissociation channels (as well is for chemical reactions).

The fragmentation of thymine, uracil and 5-bromouracil can nicely be described as a series of bond cleavages. A common fragmentation process involves several steps, a pure two-body process is very rare. Also isomerization is rare and only 5-bromouracil exhibits hydrogen migration before fragmentation. It seems that the ring itself is a very stable, rigid shape

and only after the ring has been opened, the ring parts start changing their geometry towards the most energetically favorable form. A common factor that describes the fragmentation of all the three molecules are $HNCH^+$ and $HNCO^+$ fragments, which located at the same location in all the molecules (see Fig 5.5). The fragmentation pathways of thymine, uracil and 5-

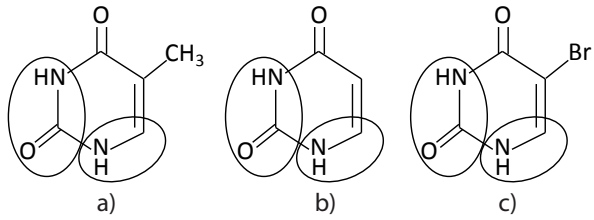

Figure 5.5: Sites of the most abundant fragments $HNCH^+$ and $HNCO^+$ resulting from C 1s core ionization of (a) thymine, (b) uracil and (c) 5-bromouracil.

bromouracil are actually mostly identical. The intensities of the corresponding fragmentation pathways do vary between the samples, but none of the molecules exhibit any drastically unique fragmentation channel. This suggests that these types of molecules, having similar ring structure, have also similar fragmentation behavior, regardless of the exocyclic functional groups attached to them.

As with acrylonitrile, the fragmentation of thymine, uracil and 5-bromouracil depend very little on the initial ionization site. The reason is probably that typically a particular Auger final state that determines the fragmentation channel can be populated from initial states with different core hole localizations, since most molecular orbitals of outer shells span the entire molecule. In addition to that, strong fragmentation pathways can occur from a number of different Auger final states (as evidenced by PEPICO measurements), which reduces the role of the initial core hole even further. This is however not the case with the weak fragmentation channels for which the dependence on the initial ionization site may be significant. A good example is the fragmentation of thymine producing $HNCOH^+$ and $C_4H_4ON^+$ coincident fragments. Figure 5.6 represents a PEPIPICO pattern corresponding to ionization of the different carbon atoms. As one can see, the pattern is really visible only when ionizing the C5 and C9; the

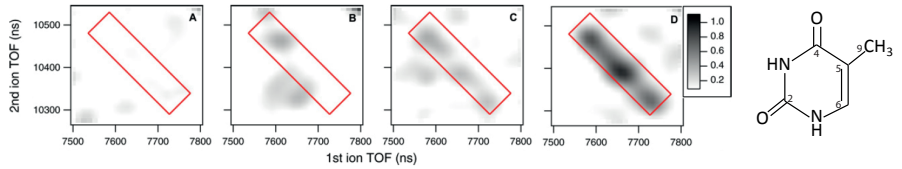

Figure 5.6: A PEPIPICO pattern corresponding to coincident fragment pair ($HNCOH^+$, $C_4H_4ON^+$); (a), (b), (c) and (d) correspond to the ionization of C2, C4, C6 and C5 + C9 respectively.

Auger final state leading to a fragmentation channels producing $HNCOH^+$ and $C_4H_4ON^+$ is possible only when the initial core hole is localized to the C5 or C9 carbons.

5.3 Photofragmentation of a nucleoside

Thymidine, a DNA nucleoside is a combination of a nucleobase, thymine, and a DNA sugar, 2-deoxy-D-ribose. The two rings are connected by a glycosidic bond between the two moieties (see Fig 5.7). The fragmentation of thymidine following valence ionization with 50 eV photons is characterized by the glycosidic bond cleavage. The energy gap between the ionization threshold and the point where the molecule begins to fragment is in the eV range. Thus even with energies below 10 eV, the molecule preferably fragments into two fragments (the sugar and the base) instead of just a singly ionized parent ion. This process involves cleavage of only one (the glycosidic) bond which, in turn, implies that there are a number of bonding orbitals just below the HOMO orbital.

Furthermore, as the energy of the incoming photon increases, more fragmentation channels become available as the photon can remove electrons from molecular orbitals also below HOMO. The number of the molecular orbitals that can be ionized with 50 eV photons is large, so the probability for ionizing the HOMO orbital and the creation of the parent ion is therefore very small. The fragmentation of thymidine following valence ionization by 50 eV photons can shortly be described as follows: the fragments larger than the base are very rare as are the small fragments with masses < 38 amu. The most common fragments are the sugar, the base and

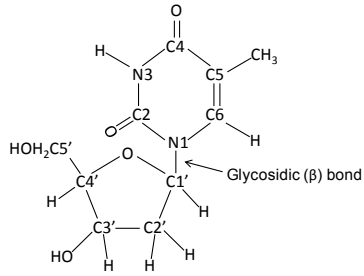

Figure 5.7: Thymidine molecule.

several other smaller fragments of the sugar part and the the fragmentation process often involves the cleavage of the glycosidic bond.

As valence ionization results into singly ionied parent molecule and the production of one charged fragment, core ionization leads to formation of two singly charged fragments. Unlike the other samples studied here, the C 1s core ionization induced fragmentation of thymidine cannot be described as a series of bond cleavages. Instead the fragmentation of thymidine is better described by different single step explosions producing the variety of detected fragments. The reason for thymidine's explosion is most likely due to its relatively unstable structure in the gas phase; the particularly weak link is the bond between the two rings. As all the other samples had a quite wide temperature gap between the sublimation temperature and thermal decomposition, with thymidine the gap is only a few dozen degrees[62]. This means that even if the thymidine molecule is intact in the gas phase, it is very fragile and needs only a small amount of additional energy to fragment. Thus, the amount of energy deposited to the thymidine molecule via core ionization is so large that the molecule cannot keep up with the following rapid geometrical changes. The parent ion then "overshoots" the achieved energy minimum and fragmentation accompanied with charge separation takes place simultaneously.

A notable difference on fragmentation following core ionization compared to fragmentation following valence ionization are the produced fragments. The coincident fragments following core ionization are essentially those with masses $\leq$43 amu, which are the weak fragments in the case of valence ionization. Also, secondary damage to living tissue is likely to be

more severe in the case of core ionization due to free ions and radicals (both neutral and charged). This is simply because, in the case of core ionization, there are more fragments, and also because Coulomb explosion gives them more energy and consequently more destructive power in secondary collisions.

5.4 Summary

The fragmentation of core ionized molecules studied here can nicely be described by sequential bond cleavages as presented in Fig. 5.1. An exception is thymidine which fragments in a single step. Several molecules exhibited nuclear rearrangement before fragmentation and charge separation which may take place in the first step of the bond cleavage process or later. The initial ionization site seems to affect the fragmentation very little as the final fragments are determined mostly by the Auger final states that may result from the multitude of initial core hole states. We also investigated simple models for estimating fragment ion abundancies without considering the details of the electronic states populated by the Auger processes. Such models do not take into account the dissociation dynamics at all and, predictably, fail in properly representing the entire fragment range. However, they give useful clues about the most abundant products and are computationally least demanding.

Since this work covered also molecules with very different geometrical structure, we can also derive some general conclusions about the effect of the molecules geometry. It has a notable effect on fragmentation; chain molecules for example have much larger tendency to fragment via two-body process, than the ring molecules among which such fragmentation channel is rare.

Bibliography

[1] A. Holden, Bonds between atoms (Oxford University Press, New York 1971).

[2] G. N. Lewis, J. Am. Chem. Soc. **38**, 762 (1916).

[3] A. Haaland, Molecules and Models: The molecular structures of main group element compounds (Oxford University Press, 2008).

[4] H. Meislich, J. Sharefkin, H. Nechamkin, G. J. Hademenos, Schaum's outlines: Organic Chemistry, 4th edition (eBook, McGraw-Hill 2010).

[5] N. L. Allinger, Molecular structure: understanding steric and electronic effects from molecular mechanics (Cambridge: Wiley-Blackwell, 2010).

[6] A. G. Turner, Methods in molecular orbital theory (Englewood Cliffs, N.J.: Prentice-Hall, 1974).

[7] R. S. Mulliken, Spectroscopy, molecular orbitals, and chemical bonding. Nobel Lecture, December 12, 1966.

[8] B. P. Straughan, S. Walker, Spectroscopy. Vol. 3. (London: Chapman and Hall, 1976).

[9] A. C. Hurley, ELectron Correlation in Small Molecules (London: Academic Press, 1976).

[10] H. Hertz, (1887) Ann. der Physik **267**, 983 (1887).

[11] P. Lenard, Ann. Physic. **8**, 149 (1902).

[12] A. Einstein, Ann. Phys. **17**, 132 (1905).

[13] A. K. Pradhan, S. N. Nahar, Atomic astrophysics and spectroscopy (Cambridge, UK; New York: Cambridge University Press, 2011.).

[14] Physical methods and molecular structure 2. 20-21, Photoelectron spectroscopy; Mass spectrometry, prepared by an Open University course team (Milton Keynes, 1977).

[15] C. R. Brundle A. D. Baker, Electron spectroscopy: theory, techniques and applications (London: Academic press, 1978).

[16] M. Weissbluth, Atoms and molecules (New York: Academic Press, 1978).

[17] J. Larmor, Phil. Mag. **44**, 503 (1897).

[18] F. R. Elder, A. M. Gurewitsch, R. V. Langmuir, H. C. Pollock, Phys Rev. **71**, 829 (1947).

[19] A. C. Thompson, D. T. Attwood, E. M. Gullikson, M. R. Howells, K-J. Kim, J. Kirz, J. B. Kortright, I. Lindau, Y. Liu, P. Pianetta, A. L. Robinson, J. H. Schofield, J. H. Underwood, G. P. Williams, X-ray data booklet (Lawrence Berkley National Laboratory, University of California, 2009).

[20] G. Margaritondo, Introduction to synchrotron radiation (New York: Oxford U.P., 1988).

[21] H. Winick, S. Doniach, Synchrotron radiation research (New York: Plenum Press, 1980).

[22] C. Kunz, Synchrotron radiation: techniques and applications (Berlin: Springer, 1979).

[23] F. Yang, J. H. Hamilton, Modern atomic and nuclear physics (Singapore; Hackensack, NJ: World Scientific, cop. 2010).

[24] http://en.wikipedia.org/wiki/File:Undulator.png.

[25] H. Kleinpoppen, M. R. C. McDowell Electron and photon interactions with atoms (New York: Plenum Press, cop. 1976).

[26] M. Bässler, A. Ausmees, M. Jurvansuu, R. Feifel, J.-O. Forsell, P. de Tarso Fonseca, A. Kivimäki, S. Sundin, S.L. Sorensen, R. Nyholm, O. Björneholm, S.Aksela, S. Svensson, Nucl. Instrum. Methods in Phys. A **469**, 382 (2001).

[27] G. LeBlanc. S. Werin, T. Meinander, H. Ahola, M. Ryynänen, J. Tahvanainen, Proceedings of EPAC 1999, see also http://www.maxlab.lu.se.

[28] M. Bässler, J.-O. Forsell, O. Björneholm, R. Feifel, M. Jurvansuu, S. Aksela, S. Sundin, S.L. Sorensen, R. Nyholm, A. Ausmees and S. Svensson, Soft X-Ray Undulator Beam Line I411 at MAX-II for Gases, Liquids and Solid Samples, J. Electron Spectrosc. Relat. Phenom. **101-103**, 953 (1999).

[29] K. Kooser, D. T. Ha, E. Itälä1, J. Laksman, S. Urpelainen, E. Kukk, J. Chem. Phys. **137**, 044304 (2012).

[30] J. F. Moulder, W. F. Stickle, P. E. Sobol, K. D. Bomber: Handbook of x-ray photoelectron spectroscopy (Minnesota: Perkin Elmer Corporation, 1992).

[31] S. Urano, X. Yand, P. R. LeBreton, J. Mol. Struct. **214**, 315 (1989).

[32] C. Nordling, E. Sokolowski, K. Siegbahn, Phys. Rev. **105**, 1676 (1957).

[33] M. Huttula, M. Harkoma, E. Nõmmiste, S. Aksela, Nucl. Nucl. Instrum. Meth. A **467**, 1514 (2001).

[34] M. Huttula, S. Heinäsmäki, H. Aksela, E. Kukk and S. Aksela, J. Electron Spectrosc. Relat. Phenom. **156-158**, 270 (2007).

[35] W. C. Wiley, I. H. McLaren, (1955) Rev. Sci. Instr. **26**, 1150 (1955).

[36] A. D. Baker, D. Betteridge, Photoelectron spectroscopy: chemical and analytical aspects (Oxford: Pergamon Press, 1972).

[37] T. A. Carlson , Photoelectron and Auger spectroscopy (New York; London, 1975).

[38] F. W. McLafferty, F. Turecek, Interpreptation of mass spectra, 4th edition (Sausalito, California: University Science Books 1993).

[39] J. T. Watson, O. D. Sparkman, Introduction to mass spectrometry: instrumentation, applications, and strategies for data interpretation, 4th edition (Hoboken, N.J.: John Wiley, 2007).

[40] C. J. Danby, J. H. D. Eland, Int. J. Mass Spectrom. and Ion Phys. **8**, 153 (1972).

[41] S. Leach, Radiat. Phys. Chem. **32**, 563 (1988).

[42] C. Miron, P. Morin, Nucl. Instrum. Meth. A **601**, 66 (2009).

[43] E. Cortés, M. F. Erben, M. Geronés, R. M. Romano, C. O. Della Védova J. Phys. Chem. A **113**, 564 (2009).

[44] J.H.D. Eland, F.S. Wort, R.N. Royds, J. Electron Spectrosc. Relat. Phenom. **41**, 297 (1986).

[45] M. Simon, T. LeBrun, P. Morin, M. Lavollée, J.L. Maréchal, Nucl. Instr. Methods B **62**, 167 (1991).

[46] L. J. Frasinski, M. Stankiewicz, K. J. Randall, P. A. Hatherly, K. Codling J. Phys. B **19** L819 (1986).

[47] C. Harada, S. Tada, K. Yamamoto, Y. Senba, H. Yoshida, A. Hiraya, S. Wada, K. Tanaka, K. Tabayashi, Rad. Phys. Chem. **75**, 2085 (2006).

[48] A. P. Hitchcock, J. J. Neville in Chemical Applications of Synchrotron Radiation, Part I: Dynamics and VUV Spectroscopy (World scientific, Singapore, 2002).

[49] K.E. McCulloch, T.E. Sharp and H.M. Rosenstock, J. Chem. Phys. **42**, 3501 (1965).

[50] J.H.D. Eland, F.S. Wort, P. Lablanquie, I. Nenner, Z. Phys. D **4**, 31 (1986).

[51] K. Ueda, H. Chiba, Y. Sato, T. Hayaishi, E. Shigemasa A. Yagishita, Phys. Rev. A **46**, R5 (1992).

[52] M. Simon, P. Morin, P. Lablanquie, M. Lavollée, K. Ueda, N. Kosugi, Chem. Phys. Lett. **238**, 42 (1995).

[53] M. Stankiewicz, P. A. Hatherly, L. J. Frasinski, K. Codling, D. M. P. Holland, J. Phys. B **22**, 21 (1989).

[54] B. Brehm, E.V. Puttkamer Z. Naturforsch. A **22**, 8 (1967).

[55] T. Baer in Gas Phase Ion Chemistry ed. by M. T. Bowers (Academic Press, New York, 1979).

[56] J. H. D. Eland, Laser Chem. **11**, 259 (1991).

[57] S. Hsieh, J. H. D. Eland, J. Chem. Phys. **103**, 1006 (1995).

[58] K. Kooser, D. T. Ha, S. Granroth, E. Itälä, L. Partanen, E. Nõmiste, H. Aksela, E. Kukk, J. Phys. B **43**, 235103 (2010).

[59] C. Miron, M. Simon, N. Leclercq, D.L. Hansen, P. Morin; Phys. Rev. Lett., **81**, 4104 (1998).

[60] S. Nagaoka, T. Fujibuchi, J. Ohshita, M. Ishikawa, I. Koyano, Int. J. Mass Spectrom. Ion Proc., **171**, 95 (1997).

[61] H. C. Schmeltz, C. Reynaud, M. Simon, I. Nenner, J. Chem. Phys., **101**, 3742 (1994).

[62] S. Ptasińska, P. Candori, S. Denifl, S. Yoon, V. Grill, P. Scheier, T.D. Märk, Chem. Phys. Lett. **409**, 270 (2005).

Original papers

The author of this thesis has participated in the measurement related to all papers except Paper I. The author carried out the data handling, analysis and the writing process (excluding those parts concerning theoretical calculations) in those papers where his name is mentioned first. In paper I, the author performed a part of the experimental data analysis.